THE JOURNAL OF PHYSICAL CHEMISTRY B

Article

Cite This: J. Phys. Chem. B 2018, 122, 229−239

pubs.acs.org/JPCB

Metastable State during Melting and Solid−Solid Phase Transition of [C_nMim][NO_3] (n = 4−12) Ionic Liquids by Molecular Dynamics Simulation

Wudi Cao,[†,‡] Yanting Wang,*[,†,‡] and Giacomo Saielli[§]

[†]CAS Key Laboratory of Theoretical Physics, Institute of Theoretical Physics, Chinese Academy of Sciences, 55 East Zhongguancun Road, P.O. Box 2735, Beijing 100190, China

[‡]School of Physical Sciences, University of Chinese Academy of Sciences, 19A Yuquan Road, Beijing 100049, China

[§]CNR Institute on Membrane Technology, Unit of Padova, Via Marzolo 1, 35131 Padova, Italy

Supporting Information

ABSTRACT: We simulate the heating process of ionic liquids [C_nMim][NO_3] (n = 4, 6, 8, 10, 12), abbreviated as C_n, by means of molecular dynamics (MD) simulation starting from a manually constructed triclinic crystal structure composed of polar layers containing anions and cationic head groups and nonpolar regions in between containing cationic alkyl side chains. During the heating process starting from 200 K, each system undergoes first a solid−solid phase transition at a lower temperature, and then a melting phase transition at a higher temperature to an isotropic liquid state (C_4, C_6, and C_8) or to a liquid crystal state (C_{10} and C_{12}). After the solid−solid phase transition, all systems keep the triclinic space symmetry, but have a different set of lattice constants. C_4 has a more significant structural change in the nonpolar regions which narrows the layer spacing, while the layer spacings of other systems change little, which can be qualitatively understood by considering that the contribution of the effective van der Waals interaction in the nonpolar regions (abbreviated as EF1) to free energy becomes stronger with increasing side-chain length, and at the same time the contribution of the effective electrostatic interaction in the polar layers (abbreviated as EF2) to free energy remains almost the same. The melting phase transitions of all systems except C_6 are found to be a two-step process with an intermediate metastable state appeared during the melting from the crystal state to the liquid or liquid crystal state. Because the contribution of EF2 to the free energy is larger than EF1, the metastable state of C_4 has the feature of having higher ordered polar layers and lower ordered side-chain orientation. By contrast, C_8−C_{12} have the feature of having lower ordered polar layers and higher ordered side-chain orientation, because for these systems, the contribution of EF2 to the free energy is smaller than EF1. No metastable state is found for C_6 because the free-energy contribution of EF1 is balanced with EF2.

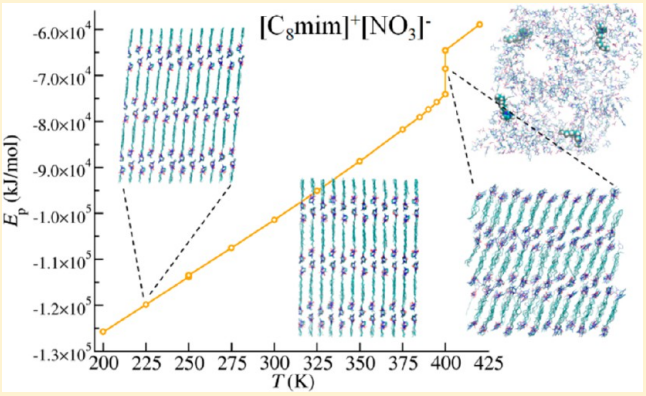

1. INTRODUCTION

Ionic liquids (ILs), molten salts whose melting temperatures are lower than 100 °C, have attracted a lot of interests over the past two decades due to their promising applications, such as green solvents, catalysts, and electrolytes.[1−7] In order to facilitate their wide applications, abundant works have been devoted to uncovering their structures in various phases, whose recent advances have been comprehensively reviewed by Atkin and co-workers.[8] However, it still lacks a systematic understanding of the phase behaviors of ILs and the associated mechanisms.

The imidazoium-based ILs, 1-alkyl-3-methylimidazolium salts, have been well-studied due to their good air and water stabilities, wide temperature range of liquid states, etc. In particular, the previous experimental investigations of [$C_n$mim][BF_4] (n = 0−18,[9] n = 12, 14, 16, and 18[10]) and [$C_n$mim][Cl] (n = 16, 18[11]) revealed that the alkyl side-chain length significantly influences the phase behavior of ILs: when the alkyl side-chain length $n \geq 12$, as the temperature T increases, the IL undergoes a phase transition from the crystal phase to the smectic ionic liquid crystal (ILC) phase, followed by a transition to the liquid phase. Similar phase behaviors were also observed by molecular dynamics (MD) simulations for [C_{16}mim] [NO_3].[12−14] Besides, cooling the ILs from the smectic phase results in a transient state related to polymorphic nucleation (n = 16, 18[11]) or a supercooled smectic phase (n = 12, 14, 16, 18[10]). When the side chain is short (n < 10), the crystal structure is either (n = 2,[15] 4[16,17]) quite different from

Received: September 12, 2017
Revised: November 19, 2017
Published: December 4, 2017

DOI: 10.1021/acs.jpcb.7b09073
J. Phys. Chem. B 2018, 122, 229−239

that of long-chain ILs ($n \geq 10$[18−21]), or absent of experimental data (n = 6,8). For n = 2−9, no ILC phase has been observed between solid and liquid, and when cooling from the liquid, they readily form glass instead of crystal.[9]

In this work, we investigate the influence of alkyl side-chain length on the phase behavior of C_4−C_{12} ILs by all-atom MD simulation. We first manually construct initial crystal structures of $[C_{12}mim][NO_3]$ according to the experimentally determined bilayer structures[18,19] and then construct shorter chain systems (n = 4,6,8,10) by truncating the side chains and re-equilibrating the system by MD simulation. This specific choice of ILs is based on the consideration that $[C_nmim][NO_3]$ have been intensively studied by MD simulation and their AMBER force fields have been verified to be eligible.[22] Our simulations have discovered a solid−solid phase transition as well as a two-step melting transition (except for $[C_6mim][NO_3]$) through a metastable state in which the system is stable for a finite time before fully melting into liquid or ILC structures. The energies, structural features, and symmetries of different phases were compared for IL systems with various alkyl side-chain lengths, based on which we propose that the increase of the van der Waals (VDW) interactions between the alkyl side chains affects the phase behavior of ILs.

2. METHODS

2.1. Simulation Setup. In the rest of this article, we will abbreviate $[C_nmim][NO_3]$ as C_n. The all-atom models of C_n and the associated force field parameters were adopted from ref 22. All simulations were performed by using the GROMACS 5.1.4 software package.[23] The simulation boxes were determined as parallelepipeds by MD simulation with the anisotropic Parrinello−Rahman barostat[24] applied, whose reference pressure was set to 1 bar. The noncubic parallelepiped shape of the simulation boxes results from the anisotropic structures of C_n commensurate with their triclinic crystal lattices. The periodic boundary condition was employed in all three dimensions and the electrostatic interactions were estimated by the Particle-mesh Ewald (PME) method.[25] Both the cutoff for the VDW interactions and the real-space cutoff for the PME were 1.2 nm. Each system contains 432 ion pairs to ensure that the simulation box is large enough for computing meaningful lattice constants.

The simulation temperature was controlled by the Nosé−Hoover thermostat.[26] The simulation processes start from the initial temperature T = 200 K and up to 10−20 K above the melting temperature by heating the system sequentially with a temperature interval of 25 K at each step, and smaller temperature intervals were applied when necessary, e.g., around the transition point. At each temperature, an MD simulation for tens to hundreds of nanoseconds was performed to equilibrate the system. The system equilibration was justified by the convergence of potential energies, structural parameters, and order parameters. A 10 ns MD simulation (20 ns near the melting point) was then followed to sample the equilibrium data. At the phase transition points when two or three phases appear at the same temperature, for each system, a single simulation of several hundred nanoseconds was performed, in which 10−50 ns was chosen for each phase to sample and calculate the ensemble-averaged thermodynamic properties separately. The VMD software[27] was used for visualizing the sampled configurations and for manual construction and adjustment of the crystalline structures.

2.2. Crystal Structure Construction. We first manually constructed the bilayer crystal structure of C_{12} and then generated crystal structures of C_{10}, C_8, C_6, and C_4 by cutting off appropriate number of carbon groups on the alkyl side chains. Each structure was repeatedly revised and refined by going through equilibration MD simulations in a wide temperature range to reach a more symmetric structure with a lower potential energy. Since no experimental data are available for the crystalline structures of imidazolium-based ILs with a nitrate anion, we compare our manually constructed structures to the experimental CCDC data with the same cations but different anions ($[C_4mim]Cl$,[16,17] $[C_{10}mim][PF_6]$,[18] $[C_{12}mim]Cl{\cdot}H_2O$[20]). By replacing their anions by nitrates at T = 10 K, we have found that our structures have a lower potential energy for C_{12} and C_{10} and a higher one for C_4 (see Table S1 in the Supporting Information). Although those results cannot unambiguously determine if our constructed structures indeed correspond to the most stable crystal structures in experiment due to the difference in anion types, the comparison shows that our manually constructed crystalline structures are reasonably good. In addition, even if some of the constructed crystalline structures are not the experimentally most favorable ones, we prefer to start from similar structures for the IL systems with different cationic side-chain lengths, since it facilitates the analysis of the influence of side-chain length on phase behaviors of ILs during heating.

2.3. Data Analysis. The energy values reported in this paper were all calculated with the GROMACS energy utility. Three key sites for each ion pair were selected for data analysis: the center-of-mass (COM) of the imidazolium ring, the COM of the anion, and the carbon atom at the end of alkyl side chain. Henceforth, we will call them headgroup, anion, and tail, respectively.

The three lattice vectors $(\vec{a},\vec{b},\vec{c})$ were obtained by solving a set of overdetermined equations

$$\vec{r}_{i'j'k'}{}^{\alpha} - \vec{r}_{ijk}^{\alpha} = (i' - i)\vec{a} + (j' - j)\vec{b} + (k' - k)\vec{c} \quad (1)$$

where the subscripts of the position vectors $\vec{r}$ are integers denoting the Bravais lattice, and the superscripts denoting a certain site type in the unit cell. In practice, we only chose the positions of head groups and anions from adjacent unit cells to construct the set of equations because of the high symmetry of the polar layers, as will be discussed later. The set of equations were solved with the common least-squares method.

To quantify different symmetries of IL systems, four types of order parameters were calculated: the translational order parameter (TOP) to quantify the translational symmetry, the orientational order parameter (OOP) to quantify the orientational symmetry, the ratio of *trans* and gauche dihedral angles[28] to quantify the conformational order of alkyl side chains, and the heterogeneity order parameter (HOP)[29] to quantify the degree of aggregation.

The TOP is defined as

$$\tau = \langle \cos(\vec{G}\cdot\Delta\vec{r}) \rangle \quad (2)$$

where $\vec{G}$ is the (1,1,1) vector in the reciprocal space and $\Delta\vec{r}$ is the vector from a site in the unit cell to its adjacent counterpart. The acute brackets represent the ensemble average taken for all possible $\Delta\vec{r}$. In this article, we will compute the TOPs for polar sites (head groups and anions) and nonpolar tails. Note that the TOP of tails also to some extent measure the conformational order of alkyl side chains. Specifically, a small TOP value

DOI: 10.1021/acs.jpcb.7b09073
J. Phys. Chem. B 2018, 122, 229−239

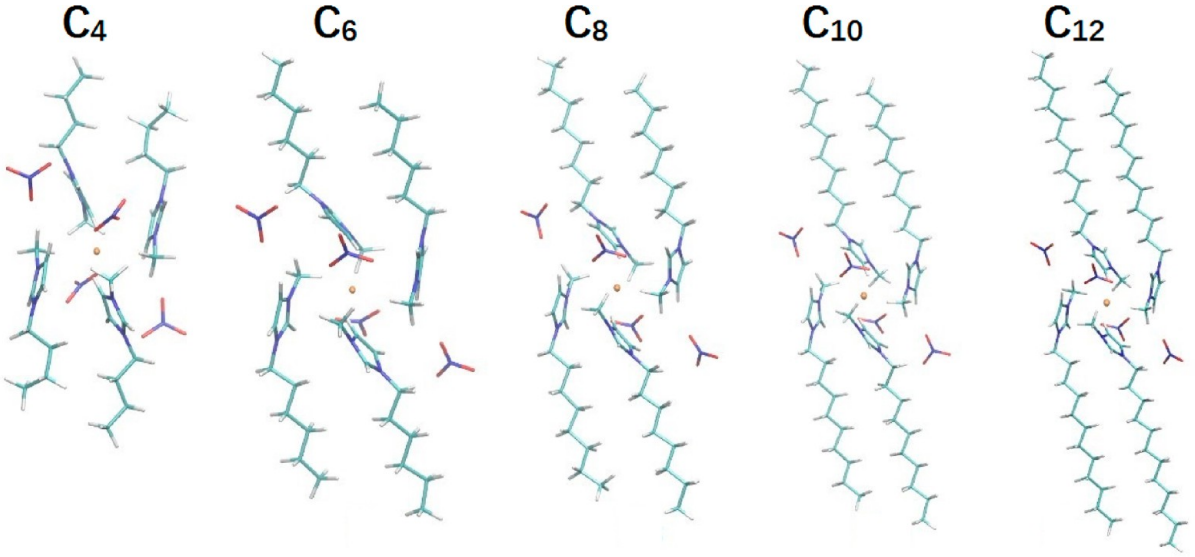

Figure 1. Snapshots of the unit cells at T = 200 K. The hydrogen atoms are in white, carbon in turquoise, nitrogen in dark blue, and oxygen in red. The golden spheres in the middle of each unit cell denote the inversion centers.

for tails indicates that the system has a distorted alkyl side-chain alignment.

The OOP for cations is defined according to the common definition for rod-like liquid crystals (LCs):[30]

$$S = \langle P_2(\cos\theta)\rangle \tag{3}$$

where θ is the angle between the global director and the directional vector of a cation pointing from the headgroup to the tail. Here the global director refers to the average orientation of all cations.

The dihedral angles defined for four subsequent bonded carbons were computed for all alkyl side chains, and the number ratios of *trans* conformations R_t and of gauche conformations R_g, defined as

$$\begin{cases} R_t = |D_t|/|D|,\ D_t = \{\phi \in D \mid \\ \qquad 150^\circ \le \phi \le 180^\circ\} \\ R_g = |D_g|/|D|,\ D_g = \{\phi \in D \mid 30^\circ \le \phi \le 90^\circ\} \end{cases} \tag{4}$$

were calculated to quantify the conformational order of alkyl side chains, where $D = \{\phi_i^j\}$ with ϕ_i^j the dihedral angle defined by C_i, ..., C_{i+3} on jth cationic alkyl side chain, and $|\cdots|$ means the cardinality.

The HOP of a single configuration is defined as

$$h = \frac{1}{N_s}\sum_{i=1}^{N_s}\sum_{j=1}^{N_s}\exp(-r_{ij}^2/2\sigma^2) \tag{5}$$

where N_s is the total number of sites, r_{ij} is the distance between sites i and j, and $\sigma = (V/N_s)^{1/3}$ which is extended from the original definition $\sigma = L/N_s^{1/3}$ for a cubic box (with a side length of L) to be applicable to a parallelepiped box. A reduced HOP $h_{reduced} = h - h_0$ is defined to allow the HOP to take a zero value when the sites are uniformly distributed. To calculate h_0 for a parallelepiped box, we placed a site at the center of the box and the other sites uniformly distributed with a distance σ, so we have

$$h_0 = \sum_{i=1}^{N_s'}\exp(-r_{0i}^2/2\sigma^2) \tag{6}$$

where r_{0i} is the distance of site i from the center of the box. Note that filling a parallelepiped box in such a way results in the number of sites N_s' in eq 6 sometimes differing from N_s, and the value of h_0 depends on the box shape, ranging from 15.5735 to 15.7435, which is slightly different from the value for a cubic simulation box reported in ref 22. From now on, we will denote the ensemble average of $h_{reduced}$ still as h for the sake of convenience. More details of the HOP can be found in the original paper.[29]

A modified TOP specifically defined for the smectic-A (SmA) liquid crystal structure is also calculated for C_{10} and C_{12} after they melt into a SmA phase, which is defined as[30]

$$\tau_{LC} = |\langle\exp(2\pi i z/d)\rangle| \tag{7}$$

where z is the z-component of the position of the polar sites and d is the layer spacing. This additional definition of TOP is necessary since eq 2 cannot be applied to a SmA phase due to the lack of a unit cell. In practice, d is also unknown and is obtained by taking the value that maximize the r.h.s in eq 7 and τ_{LC} taking the corresponding maximal value.

3. RESULTS

3.1. Crystal Structures. The constructed C_n (n = 4, 6, 8, 10, 12) crystals at low temperatures all have a triclinic lattice structure with four ion pairs in a unit cell, belonging to the $P\bar{1}$ space group which is centrosymmetric, as shown in Figure 1. Note that all alkyl side chains take the all-*trans* configurations with the only exception that a pair of chains in the unit cell of C_4 take the gauche configuration (with dihedral angles around 67°). The equilibrated configuration of C_4 has a lower potential energy than the all-*trans* configuration we have initially built, whose potential energy at T = 10 K is shown in Table S1.

The single crystal structures were constructed by duplicating the unit cells in space in such a way that the alkyl side chains align in an interdigital manner and the head groups and anions form polar bilayers inside nonpolar alkyl side-chain regions (see Figure 2). The associated lattice constants for each system

DOI: 10.1021/acs.jpcb.7b09073
J. Phys. Chem. B 2018, 122, 229−239

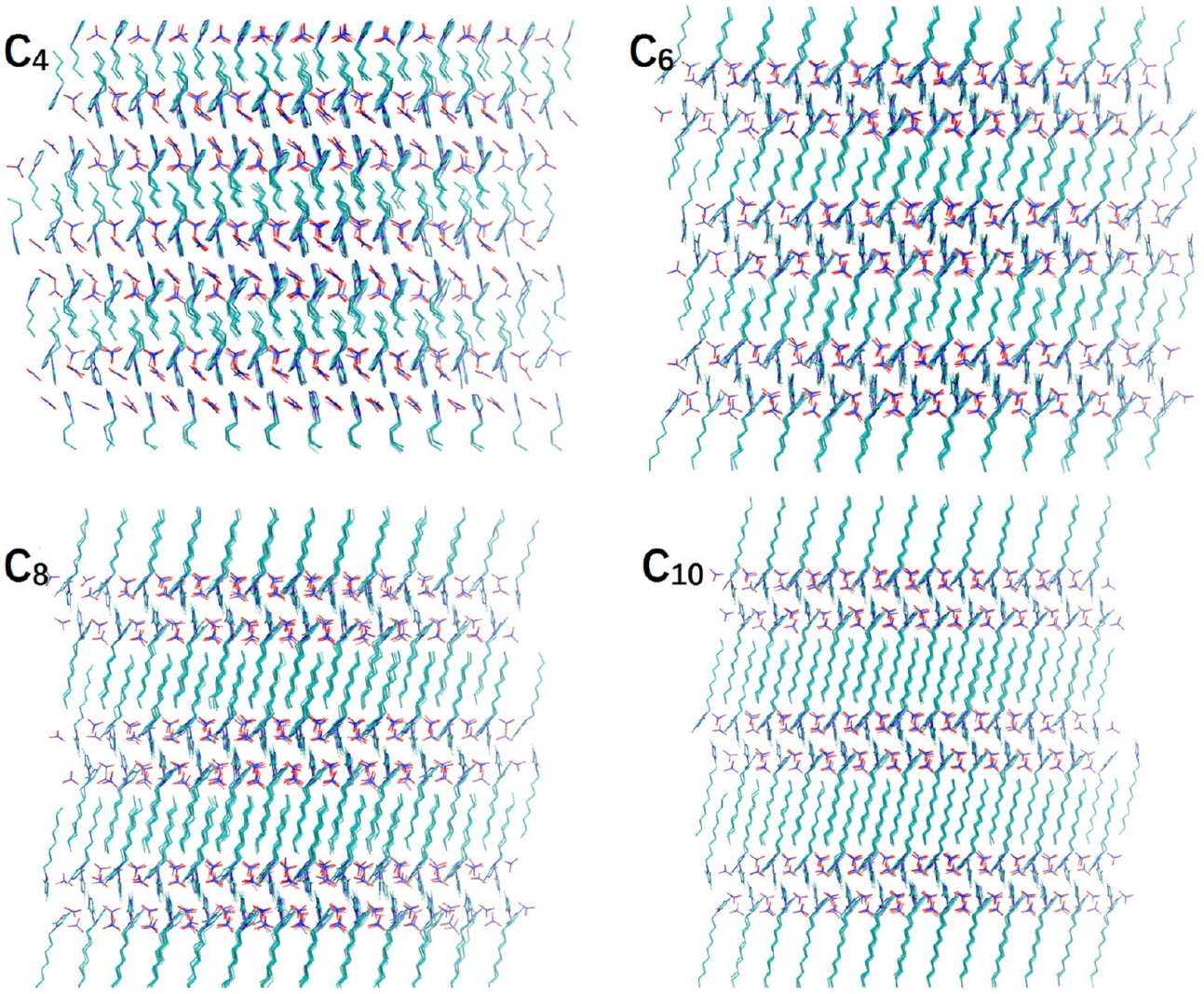

Figure 2. Snapshots of the crystal structures of C_4, C_6, C_8, and C_{10} at T = 200 K taken from the [110] direction.

Table 1. Lattice Parameters, Layer Spacings, and Densities of C_4–C_{12} at T = 200 K, with the Numbers in Brackets Being Uncertainties

	a (Å)	b (Å)	c (Å)	α (deg)	β (deg)	γ (deg)	d (Å)	ρ (g cm^{-3})
C_4	9.09(2)	8.26(2)	17.23(4)	81.3(2)	62.1(2)	67.7(2)	15.22(2)	1.264(2)
C_6	9.32(2)	8.12(2)	18.15(3)	81.2(2)	74.8(2)	73.2(2)	17.45(2)	1.204(2)
C_8	9.31(2)	8.08(1)	20.33(3)	82.1(3)	78.5(2)	73.6(2)	19.84(3)	1.194(2)
C_{10}	9.30(2)	8.04(1)	22.60(3)	82.9(2)	81.5(1)	74.0(2)	22.26(3)	1.185(2)
C_{12}	9.29(1)	8.02(1)	24.89(3)	83.6(2)	83.9(1)	74.2(1)	24.65(3)	1.179(1)

obtained at T = 200 K are listed in Table 1. The lattice vectors $\vec{a}$ and $\vec{b}$ are in the plane of polar layer and γ is the angle between them, together quantifying the structure of the polar layer. The layer spacing d is defined as the height of the unit cell vertical to the polar layer, whose value for C_{12} is in reasonable agreement with experimental results (with different anions, TFI, OTf, Br, or Cl).[31] The structures of the polar layers of C_6–C_{12} are similar and the layer spacing of C_n is 2.4 Å smaller than that of C_{n+2}. By contrast, the structure of C_4 has a different polar layer structure and its layer spacing is 2.23 Å smaller than C_6. The arrangement pattern of a polar bilayer and alkyl side chains of C_{12} are shown in Figure 3, and those for C_4–C_{10} are shown in Figure S1.

3.2. Solid–Solid Phase Transition. A solid–solid phase transition during the heating process below melting can be manifested by the kinks on the caloric curves (potential energy vs temperature) shown in Figure 4, which are 240 K for C_6, 250 K for C_8, 270 K for C_{10}, and 280 K for C_{12}. C_4 has two solid–solid phase transitions at 295 and 305 K, respectively. We compare the configurations of C_4 and C_8 before and after the solid–solid phase transitions in Figure 5 and show those of C_6, C_{10}, and C_{12} in Figure S2.

As shown in Figure 4, the jumps of potential energies of the solid–solid phase transitions are much smaller than those of melting transitions. For each system, after the solid–solid phase transition, the lattice structure is still triclinic, and the lattice parameters before and after the transitions are listed in Table 2,

DOI: 10.1021/acs.jpcb.7b09073
J. Phys. Chem. B 2018, 122, 229–239

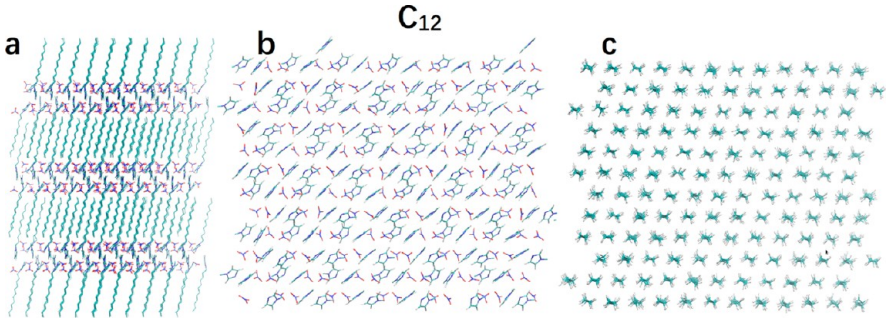

Figure 3. Snapshots of the crystal structure of C_{12} at T = 200 K taken from different perspectives: (a) from [110] direction showing the bulk structure; (b) from [001] direction showing the ordered arrangement of the polar layer; (c) from the direction along the alkyl side chains showing the arrangement of chains and their all-*trans* conformations.

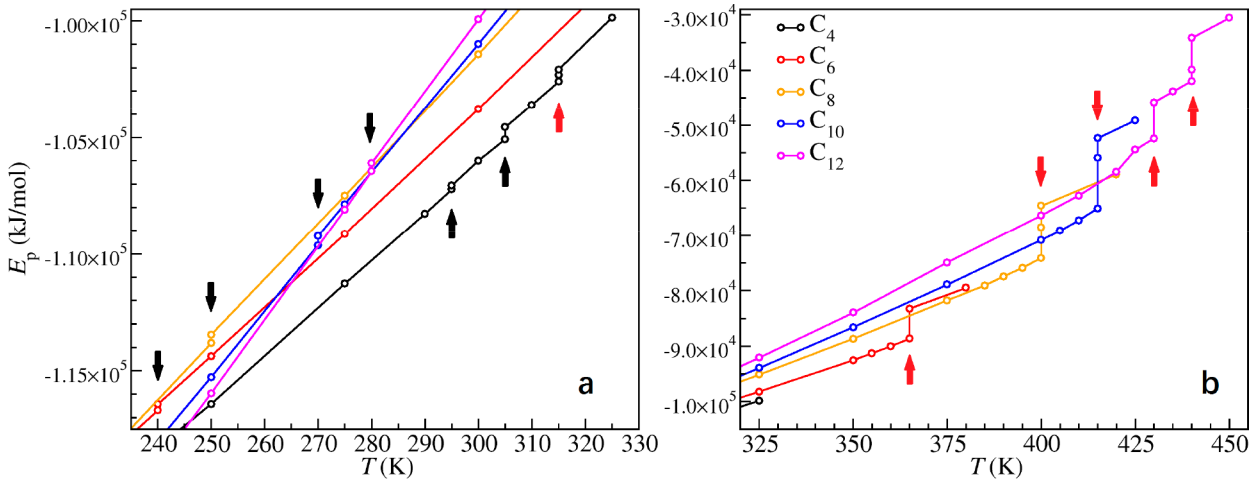

Figure 4. Caloric curves during heating. (a) From T = 240 to 325 K; (b) from T = 325 to 450 K. The solid−solid phase transition points are marked by black arrows, and the melting transition points are marked by red arrows.

with special attention on the lattice parameter γ and the layer spacing d characterizing the structures of the polar layers and of the alkyl side chains, respectively. As shown in Figure 6, for C_4, γ increases from 67.7° to 69.2° at 295 K, and to 81° at 305 K; d decreases from 15 to 14.6 Å at 295 K, and to 13.4 Å at 305 K. For C_6 to C_{12}, γ decreases from about 73° to 67° after the phase transition, and d is almost unchanged.

The calculated order parameters further distinguish the phase behavior of C_4 from other systems by more significant changes at the transition points, especially those related to alkyl side chains. As shown in Figures 7 and 8, for C_6 to C_{12}, all order parameters are almost unchanged after the solid−solid phase transition. The TOPs and OOPs remain rather high and the alkyl side chains are still basically in all-*trans* conformations, reflecting that both the polar layers and the nonpolar regions of the systems are still perfect crystals. Starting from T = 250 K, C_4 has lower TOP values for tail groups and OOP values than other systems, and the number ratios of dihedral angles deviate from 0.5, indicating that the conformations of alkyl side chains are not as ordered as those at lower temperatures. At the transition points 295 and 305 K, all the order parameters change more significantly.

The trend of solid−solid phase transition behavior of ILs with respect to the alkyl side-chain length can be qualitatively understood by considering that the contribution of the effective VDW interaction in the nonpolar regions (abbreviated as EF1) to free energy becomes stronger with increasing side-chain length while the contribution of the effective electrostatic interaction in the polar layers (abbreviated as EF2) to free energy remains almost the same. For C_4, because the alkyl side chain is short, the contribution of EF2 dominates in free energy, so during the solid−solid phase transition, the polar layers only have sight changes, but the nonpolar regions have a significant structural change. For C_6 to C_{12}, longer alkyl side chains ensure that EF1 contributes more to free energy, so both the polar layers and nonpolar regions remain a relatively high degree of structural ordering during the solid−solid phase transition.

3.3. Melting Phase Transition and Associated Metastable State. When the temperature further increases, ILs experience a melting phase transition into a liquid or ILC phase. Our simulation results indicate that the melting transition of an IL system, except C_6, takes two steps: transforming from the crystalline solid state into a metastable state before transforming into the liquid or ILC phase. As the only exception, C_6 has a melting transition taking a single step with no metastable states. As can be seen in the caloric curves in Figure 4, the melting transition points are 315 K for C_4, 365 K for C_6, 400 K for C_8, and 415 K for C_{10}. C_{12} melts into the metastable state at 430 K, which is stable for 200 ns at 430 K and subsequently another 200 ns at 435 K, before it finally melts into ILC at 440 K. In Figure 9, we show the snapshots of the metastable states of C_4 and C_8, and those for C_{10} and C_{12} are shown in Figure S3. After the melting transition, C_4, C_6, and C_8 become liquid, while C_{10} and C_{12} become ILC. The variations of order parameters with time at the melting points

DOI: 10.1021/acs.jpcb.7b09073
J. Phys. Chem. B 2018, 122, 229−239

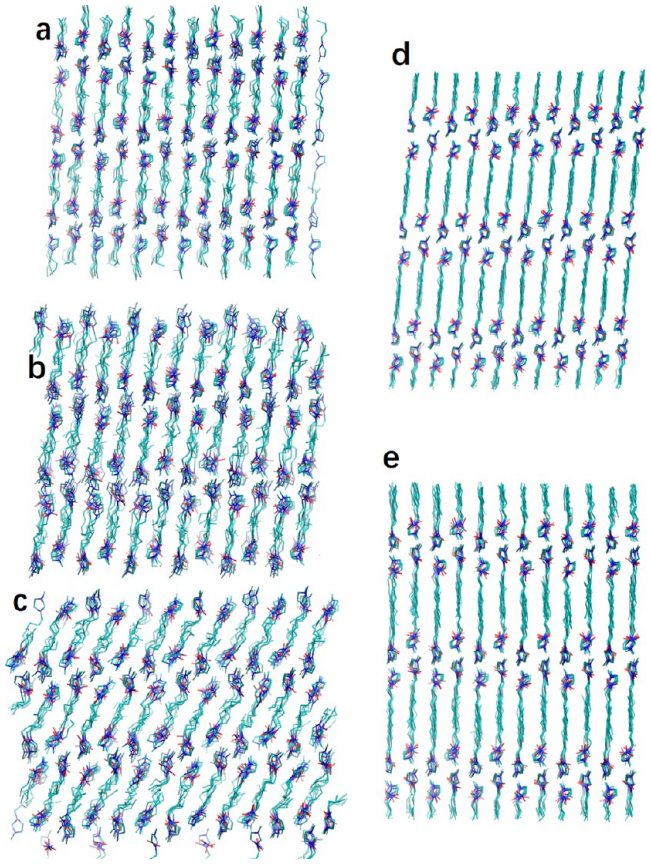

Figure 5. Snapshots of the structures before and after the solid−solid phase transitions. (a) C_4 at 295 K before the phase transition. (b) C_4 at 300 K after the first but before the second phase transition. (c) C_4 at 305 K after the phase transition. (d) C_8 at 250 K before the phase transition. (e) C_8 at 250 K after the phase transition. All these snapshots are taken from the [100] direction.

are shown in Figure S4. It is not surprising that the IL systems with longer alkyl side chains have more stable metastable states, since longer chains have stronger effect VDW interactions resulting in a higher effective energy barrier which, according to the Arrhenius law, requires more time for the system to go over and escape from the metastable structure.

The order parameters shown in Figure 7 and Figure 8 demonstrate that, during melting, the systems except C_6 can be trapped for tens to hundreds of nanoseconds in the metastable state, which still remains a certain degree of ordering inhibited from the crystal structure. For C_8, C_{10}, and C_{12}, the most noticeable difference between the crystal and metastable states is the decrease of the conformational order of alkyl side chains. The alkyl side chains no longer take the original all-*trans* conformations and many dihedral angles become gauche, meanwhile the TOP values of tail groups decrease. However, at the same time the OOP value does not change much, keeping a value larger than 0.95 for all simulated systems. In addition, the TOP values for polar sites indicate that the structure of polar layers becomes somewhat less ordered. In sum, the metastable states of C_8−C_{12} are more ordered than their liquid/ILC structures but less ordered than their crystal structures, which may have connection with the supercooled smectic phase of C_n (n = 12, 14, 16, 18) obtained experimentally.[10] For C_4, the main feature of its metastable state is that further disorder of alkyl side chains leads to the apparent decrease of OOP values while the translational order of polar sites is retained.

After a short lifetime, the metastable states eventually melt into the structures shown in Figure 10 due to the break of the intermediate interdigital structures destroyed by thermal energy. For C_4, C_6, and C_8, the cationic head groups and anions no longer form separated layers, instead they form a continuous polar network and the systems become nanosegregated liquids, as has been intensively studied in literature (see, e.g., refs 22, 29, and 32). Correspondingly, the HOP values for cationic tail groups plotted in Figure 8b indicate that tail aggregations become more apparent for longer side-chain systems, which coincides with the previous works.[22,33] For C_{10} and C_{12}, although the translational order is broken, the polar sites still form layers and the OOP also retains a high value (0.44 for C_{10} at 425 K and 0.55 for C_{12} at 450 K), demonstrating that the system structure is like the SmA phase. In addition, τ_{LC} and d of these ILC structures are also evaluated and shown as cross symbols in Figures 6b and 7a. The layer spacing d of C_{12} at T = 450 K are evaluated to be 3.23 nm, very close to the experimental values for two IL systems with the same cation but different anions (3.17 nm for Cl^- and 3.20 nm for Br^-).[31] It should be noted that in our previous simulation work,[33] C_{10} and C_{12} are found to be in liquid phase at 400 K, which does not appear in this work. This discrepancy can be explained by the fact that the liquid phase in that work was obtained by a simulated annealing procedure cooling down from a liquid phase at a high temperature, while the ILC phase

Table 2. Lattice Parameters, Layer Spacing, and Densities of C_4−C_{12} before (I) and after (II) the Solid-Solid Phase Transition Temperatures, with the Number in Brackets Being Uncertainties

		a (Å)	b (Å)	c (Å)	α (deg)	β (deg)	γ (deg)	d (Å)	ρ (g cm^{-3})
C_4 295 K	I	9.46(4)	8.43(3)	16.9(1)	78.0(5)	62.7(6)	67.7(3)	15.01(6)	1.207(3)
	II	9.58(3)	8.48(3)	16.17(7)	76.9(4)	64.9(4)	69.2(4)	14.58(5)	1.207(3)
C_4 305 K	I	9.60(3)	8.51(3)	16.11(8)	76.7(4)	65.0(4)	69.5(4)	14.53(6)	1.201(3)
	II	9.44(3)	9.06(4)	14.75(7)	76.5(4)	67.4(4)	81.0(4)	13.37(7)	1.182(3)
C_6 240 K	I	9.35(2)	8.22(2)	18.14(4)	80.9(3)	74.4(3)	72.9(2)	17.41(3)	1.192(2)
	II	9.47(3)	8.38(2)	18.46(4)	81.5(3)	70.2(2)	66.8(2)	17.36(3)	1.204(2)
C_8 250 K	I	9.35(2)	8.19(2)	20.31(3)	81.6(3)	78.2(2)	73.1(2)	19.79(3)	1.178(2)
	II	9.45(2)	8.38(2)	20.50(4)	83.6(3)	74.5(2)	67.0(2)	19.76(3)	1.187(2)
C_{10} 270 K	I	9.37(2)	8.20(2)	22.55(3)	82.0(4)	81.0(2)	73.2(3)	22.16(4)	1.162(2)
	II	9.40(2)	8.40(2)	22.70(5)	85.6(3)	78.0(2)	67.6(2)	22.20(4)	1.170(2)
C_{12} 280 K	I	9.38(2)	8.21(2)	24.80(4)	82.0(5)	83.5(2)	73.3(3)	24.48(6)	1.153(2)
	II	9.38(2)	8.40(2)	24.93(5)	87.1(3)	80.8(2)	67.9(2)	24.61(4)	1.160(2)

DOI: 10.1021/acs.jpcb.7b09073
J. Phys. Chem. B 2018, 122, 229−239

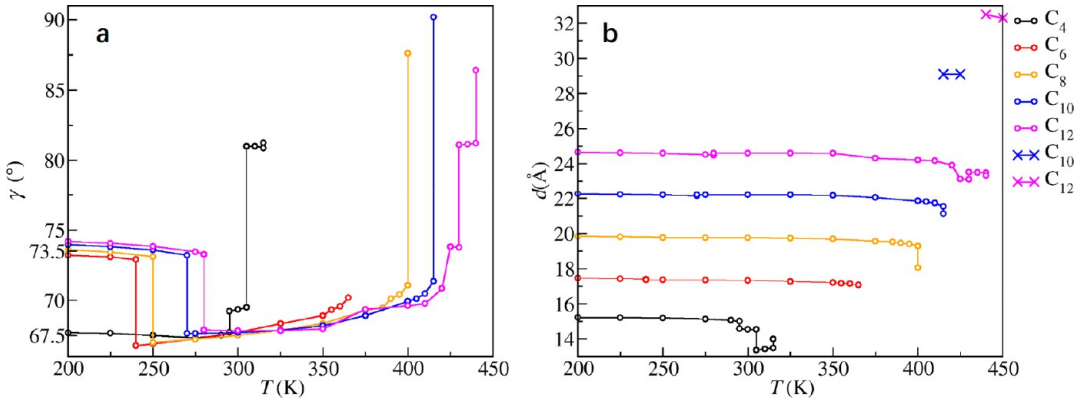

Figure 6. Deformation of unit cells during heating. (a) Angle γ between lattice vectors $\vec{a}$ and $\vec{b}$ with respect to temperature. (b) Layer spacing d with respect to temperature (cross symbols: d of SmA ILC evaluated by eq 7).

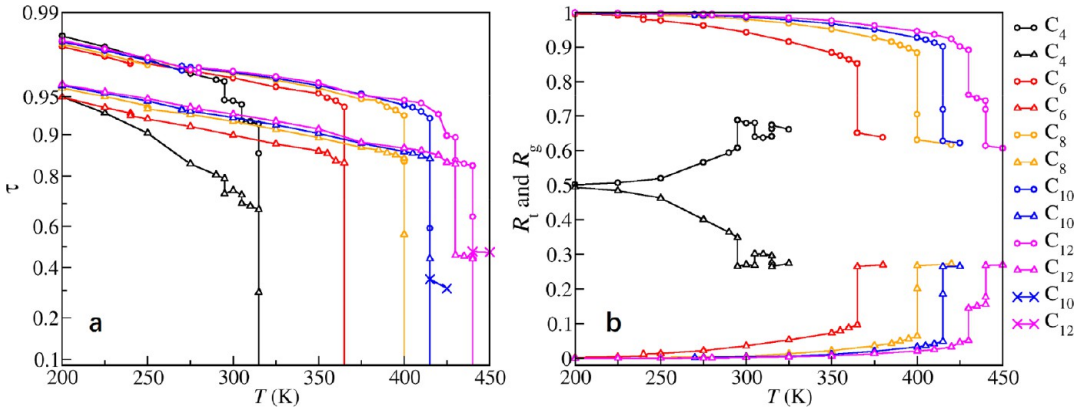

Figure 7. (a) Translational order parameters of polar bilayers (circle and cross symbols are for SmA LC evaluated by eq 7) and tails (triangle symbols). (b) Number ratios of *trans*-conformations (circle symbols) and gauche conformations (triangle symbols) versus temperature.

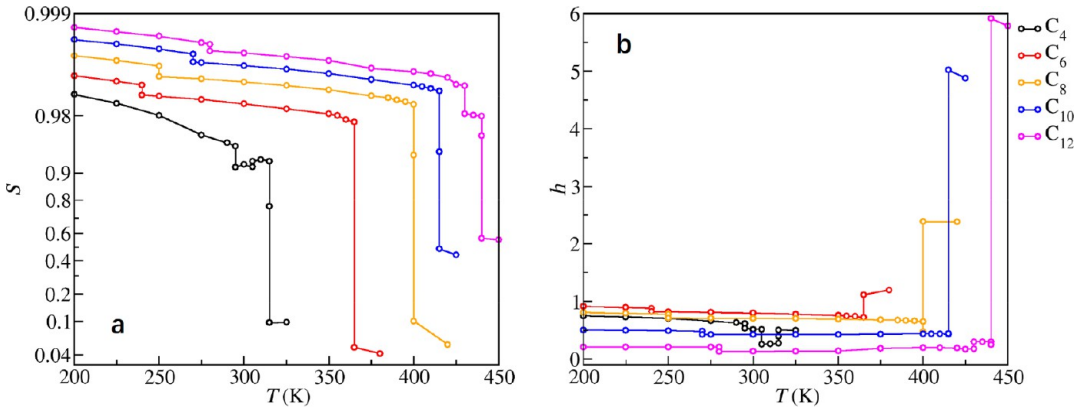

Figure 8. (a) Orientational order parameters of cations versus temperature. (b) Heterogeneity order parameters of tails versus temperature.

in this work was obtained by heating from a crystalline structure at a low temperature.

For the phase behavior of melting transition and the appearance of metastable states, we still propose a qualitative mechanism on the basis of the competition between the free-energy contributions from EF1 and EF2. For C_4, the contribution of EF2 to free energy dominates at the melting point of 315 K, so during the melting, a metastable state appears when the polar layers and nonpolar regions do not melt simultaneously, i.e., the alkyl side chains become disordered first while the polar layers still retain the ordering for a certain time. For C_8 to C_{12}, the stronger contribution of EF1 coming from the longer alkyl side chains better stabilize the bulk crystals, resulting in a melting point at 400 K or higher; when the conformations of alkyl side chains become disordered and the polar layers become less ordered at the melting points, the alkyl side chains can still retain a high orientational order for some time, leading to the metastable state during melting. For C_6, EF1 and EF2 are well balanced at the melting point of 365 K, so no metastable state appears, and the polar layers and nonpolar regions become disordered at the same time and the side chains orient isotropically.

DOI: 10.1021/acs.jpcb.7b09073
J. Phys. Chem. B 2018, 122, 229−239

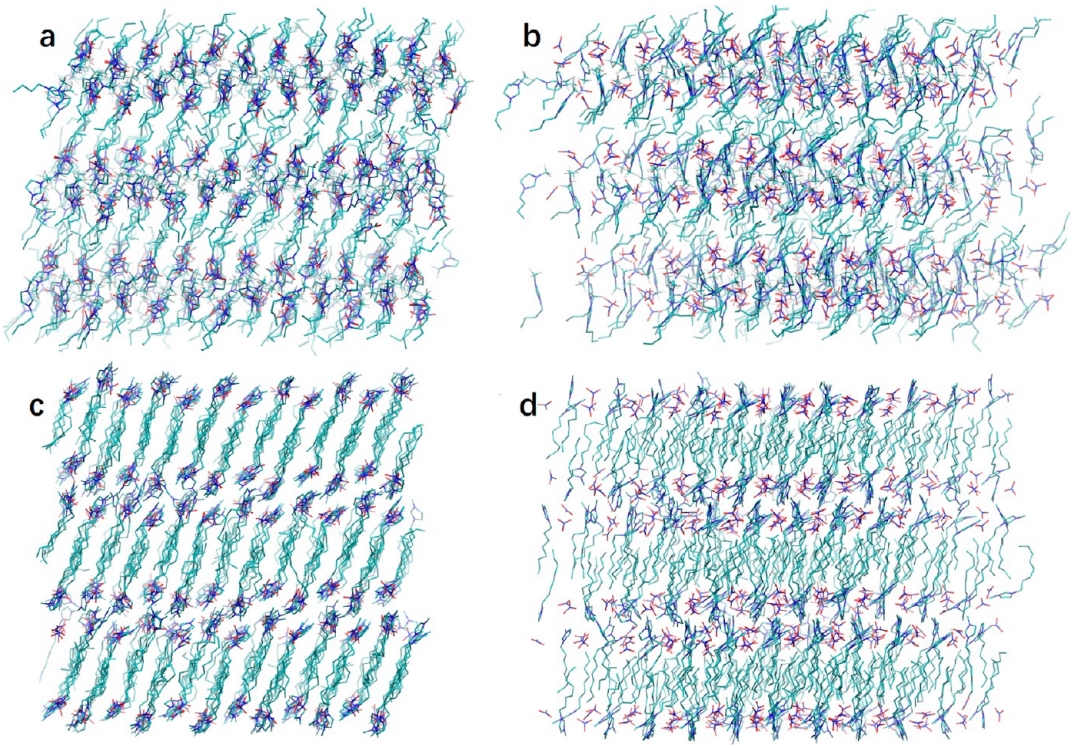

Figure 9. Snapshots of the metastable states of C_4 at T = 315 K (a) taken from the [100] direction, (b) taken from the [110] direction, and C_8 at T = 400 K (c) taken from the [100] direction, (d) taken from the [110] direction.

4. DISCUSSION

First, it should be noted that the melting points reported here are generally higher than available experimental data due to the knotty problem of superheating in MD simulation.[35] However, here we have no intention to pinpoint the very melting points by means of MD simulation, and the systematic shift of the simulated melting points to a higher temperature does no harm to the trend that the melting temperature increases with alkyl chain length, which qualitatively agrees with available experimental data for C_{10} and C_{12} with different anions.[9,34] For C_6 and C_8, only glass transition points instead of melting phase transition points are reported experimentally.[9,34] For C_4, as we have described in Section 2, the reported experimental structures[16−18] are very different from our manually constructed structure, so the experimental melting points cannot directly compare with our results.

To see if the solid−solid phase transition we have observed has the limitation of starting from a specific manually constructed IL structure, we construct an experimentally reported monoclinic structure for $[C_{10}MIM][PF_6]$[18,36] (Figure S5a), and then replace the anions by nitrates to obtain a new crystal structure for $[C_{10}MIM][NO_3]$. After proper equilibration at 10 K, the new structure of $[C_{10}MIM][NO_3]$ has a higher potential energy than our manually constructed structure, as reported in Section 2. Conversely, we replace the nitrates in our manually constructed $[C_{10}MIM][NO_3]$ structure by PF_6. After proper equilibration at 10 K, the new structure (Figure S5b) has a lower potential energy than the experimental monoclinic structure. Therefore, we are sure that the experimental crystal structure of $[C_{10}MIM][PF_6]$ measured at 173 K is a one already going through the solid−solid phase transition at a lower temperature, which seems to imply that solid−solid phase transition is a general feature for IL systems.

The same heating MD simulation procedure described in Section 2 has also been applied to the $[C_{12}MIM][Cl]\cdot H_2O$ system starting from an experimental triclinic structure.[20] From Figures S6, S7, and Table S2, we can clearly see that the system goes through a distinct solid−solid phase transition at 375 K when the lattice constant α changes abruptly while the layer spacing almost remains the same. It traps in a metastable state at 400 K before melting into the liquid crystal at 410 K. These results further support our proposed mechanisms for the solid−solid phase transition and the metastable state during melting in IL systems.

5. CONCLUSIONS

In this work, we constructed the initial crystal structures for $[C_n mim][NO_3]$ ILs (n = 4,6,8,10,12). These crystal structures have distinct polar layers composed of cationic head groups and anions and nonpolar regions composed of cationic alkyl side chains. Then we studied the phase behaviors by means of MD simulation by heating these crystals from 200 K until 10−20 K above the melting point, at which they are in liquid or liquid crystal phase. During heating in MD simulations, we observed solid−solid phase transitions and two-step melting transitions with a metastable state (except C_6 whose melting transition is one-step without the metastable state).

The alkyl side-chain length of cation has a strong influence on both phase transitions. Specifically, the solid−solid phase transitions of C_6 to C_{12} are similar and the transition temperature increases with the alkyl side-chain length n. During this transition, the polar layer structures of these systems are always similar and their layer spacings have little change. Comparatively, C_4 has two subsequent solid−solid phase transitions, the layer spacing evidently narrows after the transitions, and the transition temperatures are higher than that of C_{12}. The solid−solid phase transitions for those IL systems

DOI: 10.1021/acs.jpcb.7b09073
J. Phys. Chem. B 2018, 122, 229−239

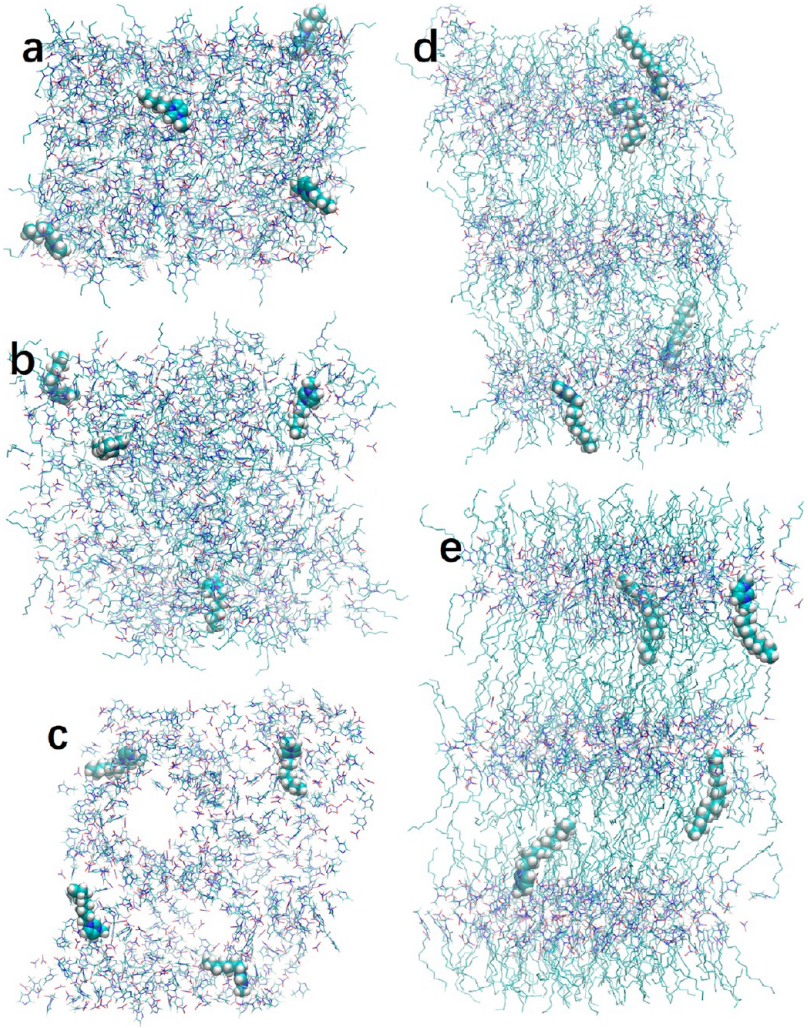

Figure 10. Snapshots of the melted phases. (a) Liquid structure of C_4 at 325 K. (b) Liquid structure of C_6 at 380 K. (c) Liquid structure of C_8 at 420 K without showing the aggregated alkyl side chains. (d) ILC structure of C_{10} at 425 K. (e) ILC structure of C_{12} at 450 K.

can be qualitatively understood by considering that the contribution of the effective VDW interaction in the nonpolar regions (EF1) to free energy becomes stronger with increasing side-chain length, while the contribution of the effective electrostatic interaction in the polar layers (EF2) to free energy remains almost the same. For C_4, EF1 is weak, so the alkyl side-chains have less ordered conformations and tilt more after the transitions, and thus the layer spacing decreases correspondingly. For C_6–C_{12}, both EF1 and EF2 are strong enough to keep the polar layers and nonpolar regions ordered and the layer spacing is basically unchanged after the transition.

As for the melting transitions, C_6 directly melts into liquid while other systems first stay in the metastable state for tens to hundreds of nanoseconds before melt into a liquid or ILC state, and the melting temperature increases as the alkyl side chains become longer. As for the metastable state, the polar layers of C_4 have a higher order than other systems, while the orientational order of the nonpolar alkyl side-chain region for C_8, C_{10}, or C_{12} is more ordered than C_4. Finally, C_4 to C_8 melt into the nanosegregation liquid state, while C_{10} and C_{12} melt into the SmA ILC phase due to the remaining order of the nonpolar alkyl side-chain regions. The melting transitions can also be qualitatively understood by the competition between the free-energy contributions from EF1 and EF2. For C_4, EF1 is weaker than EF2 at the melting point of 315 K, so the alkyl side chains lose the crystalline order before the polar layers do. For C_8 to C_{12}, EF1 becomes stronger with longer alkyl side chains, resulting in increasing melting temperatures ($T \geq 400$ K), at which the alkyl side chains keep their orientations uniform for a certain time despite the fact that alkyl side chains and polar layers no longer stay in their lattice positions. For C_6, EF1 is well balanced with EF2 at the melting point of 365 K, so both the polar layers and nonpolar alkyl side chains melt simultaneously without the appearance of a metastable state.

It would be nice if we could quantify the contributions of EF1 and EF2 to free energy. However, it is not an easy task because (1) it is not obvious how to extract the effective VDW interaction between cationic side chains and the effective electrostatic interaction between polar groups (cationic head groups and anions) from the simulation data, and (2) it is free energy rather than potential energy contributions which determine the phase behavior of the IL systems, but calculating free energy based on simulation data is notoriously difficult. Therefore, in this article, we only provide a phenomenological qualitative microscopic mechanism from the viewpoint of statistical physics, and constructing a quantitative statistical model for the proposed mechanism will be our next research topic.

DOI: 10.1021/acs.jpcb.7b09073
J. Phys. Chem. B 2018, 122, 229–239

■ ASSOCIATED CONTENT

Supporting Information

The Supporting Information is available free of charge on the ACS Publications website at DOI: 10.1021/acs.jpcb.7b09073.

Table for the comparison of potential energies of crystal structures, more snapshots of crystals and metastable states, and plots of order parameters versus time at melting points (PDF)

■ AUTHOR INFORMATION

Corresponding Author

*E-mail: wangyt@itp.ac.cn

ORCID

Wudi Cao: 0000-0002-3410-3708

Giacomo Saielli: 0000-0003-3337-8395

Notes

The authors declare no competing financial interest.

■ ACKNOWLEDGMENTS

This work was supported by the National Natural Science Foundation of China (Nos. 11774357 and 11421063). The computations of this work were conducted on the HPC cluster of ITP-CAS and on the Tianhe-2 supercomputer. We also thank the CNR-CAS 2017-2019 bilateral agreement for support. This work was partly supported by the Chinese Academy of Sciences through the CAS President's International Fellowship Initiative (No.2017VMC0005) to GS and the CAS Biophysics Interdisciplinary Innovation Team Project (No. 2060299) to Y.W.

■ ABBREVIATIONS

IL: ionic liquid; LC: liquid crystal; ILC: ionic liquid crystal; MD: molecular dynamics; VDW: van der Waals; TOP: translational order parameter; OOP: orientational order parameter; HOP: heterogeneity order parameter; EF1: effective VDW interaction in nonpolar regions; EF2: effective electrostatic interaction in polar layers

■ REFERENCES

(1) Rogers, R. D.; Seddon, K. R. Ionic Liquids–Solvents of the Future? *Science* **2003**, *302*, 792−793.

(2) Swatloski, R. P.; Spear, S. K.; Holbrey, J. D.; Rogers, R. D. Dissolution of Cellose with Ionic Liquids. *J. Am. Chem. Soc.* **2002**, *124*, 4974−4975.

(3) Zhao, D.; Wu, M.; Kou, Y.; Min, E. Ionic Liquids: Applications in Catalysis. *Catal. Today* **2002**, *74*, 157−189.

(4) Galiński, M.; Lewandowski, A.; Stępniak, I. Ionic Liquids as Electrolytes. *Electrochim. Acta* **2006**, *51*, 5567−5580.

(5) Greaves, T. L.; Drummond, C. J. Protic Ionic Liquids: Properties and Applications. *Chem. Rev.* **2008**, *108*, 206−237.

(6) Plechkova, N. V.; Seddon, K. R. Applications of Ionic Liquids in the Chemical Industry. *Chem. Soc. Rev.* **2008**, *37*, 123−150.

(7) Olivier-Bourbigou, H.; Magna, L.; Morvan, D. Ionic Liquids and Catalysis: Recent Progress from Knowledge to Applications. *Appl. Catal., A* **2010**, *373*, 1−56.

(8) Hayes, R.; Warr, G. G.; Atkin, R. Structure and Nanostructure in Ionic Liquids. *Chem. Rev.* **2015**, *115*, 6357−6426.

(9) Holbrey, J. D.; Seddon, K. R. The Phase Behaviour of 1-Alkyl-3-Methylimidazolium Tetrafluoroborates; Ionic Liquids and Ionic Liquid Crystals. *J. Chem. Soc., Dalton Trans.* **1999**, 2133−2140.

(10) Nozaki, Y.; Yamaguchi, K.; Tomida, K.; Taniguchi, N.; Hara, H.; Takikawa, Y.; Sadakane, K.; Nakamura, K.; Konishi, T.; Fukao, K. Phase Transition and Dynamics in Imidazolium-Based Ionic Liquid Crystals through a Metastable Highly Ordered Smectic Phase. *J. Phys. Chem. B* **2016**, *120*, 5291−5300.

(11) Li, L.; Groenewold, J.; Picken, S. J. Transient Phase-Induced Nucleation in Ionic Liquid Crystals and Size-Frustrated Thickening. *Chem. Mater.* **2005**, *17*, 250−257.

(12) Saielli, G. MD Simulation of the Mesomorphic Behaviour of 1-Hexadecyl-3-Methylimidazolium Nitrate: Assessment of the Performance of a Coarse-Grained Force Field. *Soft Matter* **2012**, *8*, 10279−10287.

(13) Saielli, G.; Voth, G. A.; Wang, Y. Diffusion Mechanisms in Smectic Ionic Liquid Crystals: Insights from Coarse-Grained MD Simulations. *Soft Matter* **2013**, *9*, 5716−5725.

(14) Saielli, G.; Bagno, A.; Wang, Y. Insights on the Isotropic-to-Smectic a Transition in Ionic Liquid Crystals from Coarse-Grained Molecular Dynamics Simulations: The Role of Microphase Segregation. *J. Phys. Chem. B* **2015**, *119*, 3829−3836.

(15) Wilkes, J. S.; Zaworotko, M. J. Air and Water Stable 1-Ethyl-3-Methylimidazolium Based Ionic Liquids. *J. Chem. Soc., Chem. Commun.* **1992**, 965−967.

(16) Holbrey, J. D.; Reichert, W. M.; Nieuwenhuyzen, M.; Johnson, S.; Seddon, K. R.; Rogers, R. D. Crystal Polymorphism in 1-Butyl-3-Methylimidazolium Halides: Supporting Ionic Liquid Formation by Inhibition of Crystallization. *Chem. Commun.* **2003**, 1636−1637.

(17) Saha, S.; Hayashi, S.; Kobayashi, A.; Hamaguchi, H. Crystal Structure of 1-Butyl-3-Methylimidazolium Chloride. A Clue to the Elucidation of the Ionic Liquid Structure. *Chem. Lett.* **2003**, *32*, 740−741.

(18) Reichert, W. M.; Holbrey, J. D.; Swatloski, R. P.; Gutowski, K. E.; Visser, A. E.; Nieuwenhuyzen, M.; Seddon, K. R.; Rogers, R. D. Solid-State Analysis of Low-Melting 1,3-Dialkylimidazolium Hexafluorophosphate Salts (Ionic Liquids) by Combined X-Ray Crystallographic and Computational Analyses. *Cryst. Growth Des.* **2007**, *7*, 1106−1114.

(19) Gordon, C. M.; Holbrey, J. D.; Kennedy, A. R.; Seddon, K. R. Ionic Liquid Crystals: Hexafluorophosphate Salts. *J. Mater. Chem.* **1998**, *8*, 2627−2636.

(20) Guillet, E.; Imbert, D.; Scopelliti, R.; Bünzli, J.-C. G. Tuning the Emission Color of Europium-Containing Ionic Liquid-Crystalline Phases. *Chem. Mater.* **2004**, *16*, 4063−4070.

(21) De Roche, J.; Gordon, C. M.; Imrie, C. T.; Ingram, M. D.; Kennedy, A. R.; Lo Celso, F.; Triolo, A. Application of Complementary Experimental Techniques to Characterization of the Phase Behavior of [C16mim][PF6] and [C14mim][PF6]. *Chem. Mater.* **2003**, *15*, 3089−3097.

(22) Wang, Y.; Jiang, W.; Voth, G. A., Spatial Heterogeneity in Ionic Liquids. In *Ionic Liquids IV*; American Chemical Society, 2007; Vol. *975*, pp 272−307.

(23) Abraham, M. J.; Murtola, T.; Schulz, R.; Páll, S.; Smith, J. C.; Hess, B.; Lindahl, E. Gromacs: High Performance Molecular Simulations through Multi-Level Parallelism from Laptops to Supercomputers. *SoftwareX* **2015**, *1−2*, 19−25.

(24) Parrinello, M.; Rahman, A. Polymorphic Transitions in Single Crystals: A New Molecular Dynamics Method. *J. Appl. Phys.* **1981**, *52*, 7182−7190.

(25) Darden, T.; York, D.; Pedersen, L. Particle Mesh Ewald: An N·Log(N) Method for Ewald Sums in Large Systems. *J. Chem. Phys.* **1993**, *98*, 10089−10092.

(26) Nosé, S. A Molecular Dynamics Method for Simulations in the Canonical Ensemble. *Mol. Phys.* **1984**, *52*, 255−268.

(27) Humphrey, W.; Dalke, A.; Schulten, K. VMD: Visual Molecular Dynamics. *J. Mol. Graphics* **1996**, *14*, 33−38.

(28) McNaught, A. D.; Wilkinson, A. *IUPAC. Compendium of Chemical Terminology*, 2nd ed.; Blackwell Scientific Publications: Oxford, U.K., 1997.

(29) Wang, Y.; Voth, G. A. Tail Aggregation and Domain Diffusion in Ionic Liquids. *J. Phys. Chem. B* **2006**, *110*, 18601−18608.

(30) Bates, M. A.; Luckhurst, G. R. Computer Simulation Studies of Anisotropic Systems. XXX. The Phase Behavior and Structure of a Gay−Berne Mesogen. *J. Chem. Phys.* **1999**, *110*, 7087−7108.

(31) Bradley, A. E.; Hardacre, C.; Holbrey, J. D.; Johnston, S.; McMath, S. E. J.; Nieuwenhuyzen, M. Small-Angle X-Ray Scattering Studies of Liquid Crystalline 1-Alkyl-3-Methylimidazolium Salts. *Chem. Mater.* **2002**, *14*, 629−635.
(32) Canongia Lopes, J. N. A.; Pádua, A. A. H. Nanostructural Organization in Ionic Liquids. *J. Phys. Chem. B* **2006**, *110*, 3330−3335.
(33) Ji, Y.; Shi, R.; Wang, Y.; Saielli, G. Effect of the Chain Length on the Structure of Ionic Liquids: From Spatial Heterogeneity to Ionic Liquid Crystals. *J. Phys. Chem. B* **2013**, *117*, 1104−1109.
(34) Holbrey, J. D.; Seddon, K. R. Ionic Liquids. *Clean Technol. Environ. Policy* **1999**, *1*, 223−236.
(35) Zhang, Y.; Maginn, E. J. Molecular Dynamics Study of the Effect of Alkyl Chain Length on Melting Points of [Cnmim][Pf6] Ionic Liquids. *Phys. Chem. Chem. Phys.* **2014**, *16*, 13489−99.
(36) Canongia Lopes, J. N.; Pádua, A. A. Molecular Force Field for Ionic Liquids Composed of Triflate or Bistriflylimide Anions. *J. Phys. Chem. B* **2004**, *108*, 16893−16898.

DOI: 10.1021/acs.jpcb.7b09073
J. Phys. Chem. B 2018, 122, 229−239